

SuperPhys-Net: A Physics-Informed Super-Resolution Electromagnetic Simulator for Nanophotonic Devices

Yiyang Su
HKUST(GZ)

Hao Chen
HKUST(GZ)

Guohao Dai
HKUST(GZ)

Yuzhe Ma
HKUST(GZ)

Yeyu Tong
HKUST(GZ)

Abstract—The rapid advancement of photonic integrated circuits is driving innovations in interconnect, computing, and sensing applications. This progress has led to the development of nanophotonic waveguide devices with complex geometries, offering greater design flexibility and a wider range of functional applications. However, electromagnetic (EM) simulation imposes a heavy computational burden during the design and validation phases. This significantly hampers design iteration speed and scalability. Although existing data-driven methods and physics-informed neural networks have shown promise for simpler structures, they fall short for highly complex geometries, limiting the automation of photonic device design. To address these issues, we present the SuperPhys-Net framework. This innovative approach enhances coarse-grid simulation results through super-resolution and integrates physical constraints to generate fine-grid solutions that adhere to physical laws. Our model demonstrates outstanding performance across complex nanophotonic waveguide devices with varying dimensions, achieving a 72.61% improvement in accuracy over current state-of-the-art models. Additionally, it reduces computational time by 76.09% compared to standard finite-difference frequency-domain solvers, all while maintaining exceptional accuracy across all scales.

I. INTRODUCTION

Photonic integrated circuits (PICs) are increasingly essential for next-generation applications in communications, quantum computing, imaging, and sensing [1]–[3]. The escalating complexity and performance requirements have exposed the limitations of current integrated photonic components, driving the need for nanophotonic waveguide devices that provide multifunctionality in an extremely compact footprint. Achieving this goal poses significant challenges for traditional photonic design methods.

In contrast to traditional devices that rely on size and shape optimization, nanophotonic devices that utilize topology optimization offer a significantly greater degree of freedom, as shown in Fig. 1(a). This increased degree of freedom allows designers to explore broader design spaces and achieve more refined control over light-matter interactions at the nanoscale, resulting in improved device performance and enhanced design flexibility [4]. By integrating automated design algorithms with topology optimization techniques, researchers have successfully created a variety of nanophotonic devices that demonstrate exceptional performance. Examples of these devices, depicted in Fig. 1(b), include wavelength

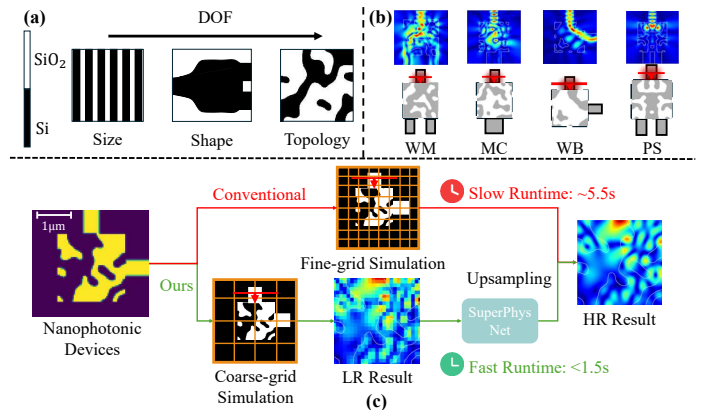


Fig. 1: (a) Top view of integrated photonic devices employing various design approaches, illustrating differing degrees of freedom (DOF). (b) Examples of nanophotonic devices using topology structure design, including wavelength multiplexers (WM), power splitters (PS), waveguide bends (WB), and mode converters (MC), along with their corresponding simulated electromagnetic field distributions. (c) Comparison of our proposed SuperPhys-Net framework with conventional standard finite-difference frequency-domain (FDFD) simulations. HR: high-resolution, LR: low-resolution.

multiplexers, power splitters, waveguide bends, and mode converters, and many others [5]–[8].

The design process for nanophotonic devices often necessitates extensive electromagnetic (EM) simulations for iterative optimization, which constitutes the primary computational and time burden. This significantly impedes rapid design iterations and large-scale optimization efforts [9], [10]. Consequently, the development of efficient methods for accelerating EM simulations has become essential for enhancing nanophotonic device design. Current methods for accelerating EM simulations can be categorized into two main types: data-driven approaches and physics-informed neural networks (PINNs). Data-driven methods, particularly neural operators, achieve EM simulation acceleration by learning the mapping between input parameters and optical field responses. These approaches have demonstrated successful acceleration of EM simulations for multi-mode interference devices, metaline structures, and micro-ring resonators [11]–[13]. On the other hand, PINNs

incorporate Maxwell’s equations directly into the training of neural networks, utilizing these physical principles as constraints [14]. This approach has been effectively applied in the design of micro-lenses and grating couplers [15], [16]. However, both acceleration methods face significant challenges when applied to nanophotonic devices with complex topological structures. Data-driven methods struggle with generalization to new topologies beyond their training data and require exponentially larger datasets as device complexity increases, potentially yielding physically inconsistent results that violate fundamental EM principles. Although PINNs enforce physical equations in their predictions, they encounter difficulties in dealing with irregular geometric boundaries and significant variations in refractive indices typical of complex topological nanophotonic devices, often resulting in convergence problems and diminished accuracy in capturing complex EM phenomena.

To address the simulation challenges of nanophotonic devices with complex topological structures, we propose SuperPhys-Net, a physics-informed super-resolution (SR) EM simulator. The main contributions are summarized as follows:

- We propose a novel EM simulation framework for nanophotonic devices with arbitrary geometries. This framework learns the mapping from coarse-grid to fine-grid EM fields, achieving a 76.09% computational time reduction compared to standard Finite-Difference Frequency-Domain (FDFD) solvers and a 72.61% accuracy improvement relative to current state-of-the-art simulation acceleration techniques.
- We integrate Maxwell’s equations as physical constraints into the SR framework, ensuring EM field consistency and further improving accuracy by 9.84% compared to conventional data-driven SR methods.
- Our method consistently demonstrates significantly lower prediction errors when compared to other baseline models across a range of nanophotonic devices with different minimum feature sizes and spacing values, indicating its exceptional generalizability for multifunctional nanophotonic device simulations.

II. PRELIMARIES

A. EM Simulation

EM simulation can be fundamentally viewed as solving partial differential equations that govern EM wave propagation. Traditional numerical methods, such as the Finite-Difference Time-Domain (FDTD) and Finite-Difference Frequency-Domain (FDFD) methods, discretize Maxwell’s equations into large linear systems, which are computationally expensive to solve, particularly when high spatial resolution is required. Maxwell’s equations in the frequency domain can be expressed in the form:

$$(\mu^{-1}\nabla \times \nabla \times - \omega^2\epsilon_0\epsilon_r(\mathbf{r})) \mathbf{E}(\mathbf{r}) = j\omega\mathbf{J}(\mathbf{r}) \quad (1)$$

where $\mathbf{E}(\mathbf{r})$ represents the electric field, ϵ_0 is the vacuum permittivity, $\epsilon_r(\mathbf{r})$ is the relative permittivity distribution defining

the device geometry, μ is the permeability, $\mathbf{J}(\mathbf{r})$ is the current source, and ω is the angular frequency.

B. Super Resolution Techniques

SR techniques, which enhance low-resolution (LR) data to high-resolution (HR) outputs through deep learning, have achieved remarkable success across diverse scientific domains, including fluid dynamics [17], [18], remote sensing [19]–[21], and climate modeling [22], [23]. Common SR approaches can be broadly categorized into several types: traditional interpolation methods such as bicubic and bilinear interpolation, regression-based methods that learn mappings from LR to HR data through convolutional neural networks, generative adversarial networks that employ adversarial training to produce more realistic high-frequency details, and diffusion models that iteratively refine outputs through denoising processes [24]–[26].

In EM simulation, SR has been successfully applied to 2D grating arrays and antenna modeling [27], [28], demonstrating significant computational acceleration. However, these existing approaches are purely data-driven, requiring extensive training datasets and often producing results that violate fundamental physical laws due to a lack of physics constraints.

III. PROPOSED METHOD

A. From Coarse to Fine Grid: EM Field Super-Resolution

The application of SR to EM field prediction exploits the inherent trade-off in numerical EM solvers between grid resolution and computational cost. Coarser grids reduce complexity but introduce discretization errors, while finer grids minimize errors at significantly increased simulation time.

In numerical EM simulation, the continuous spatial domain is discretized into a finite grid with spatial steps Δx and Δy , which determine the grid resolution. Smaller grid steps (finer grids) provide higher spatial resolution and better accuracy, but at the cost of significantly increased computational time and memory requirements. Conversely, larger grid steps (coarser grids) reduce computational burden but introduce discretization errors that can affect simulation accuracy. For 2D TM mode problems, the wave equation is given by:

$$\nabla^2 E_z + k_0^2 \epsilon_r E_z = -j\omega\mu_0 J_z \quad (2)$$

where E_z is the z -component of the electric field, $k_0 = \omega/c$ is the free-space wavenumber, ϵ_r is the relative permittivity, μ_0 is the vacuum permeability, J_z is the z -component of the current source, and ω is the angular frequency. Using finite-difference discretization:

$$\begin{aligned} & \frac{E_z(i+1, j) - 2E_z(i, j) + E_z(i-1, j)}{(\Delta x)^2} \\ & + \frac{E_z(i, j+1) - 2E_z(i, j) + E_z(i, j-1)}{(\Delta y)^2} \\ & + k_0^2 \epsilon_r(i, j) E_z(i, j) = -j\omega\mu_0 J_z(i, j) \end{aligned} \quad (3)$$

where (i, j) represents the grid indices, and Δx , Δy are the spatial discretization steps in the x and y directions, respectively.

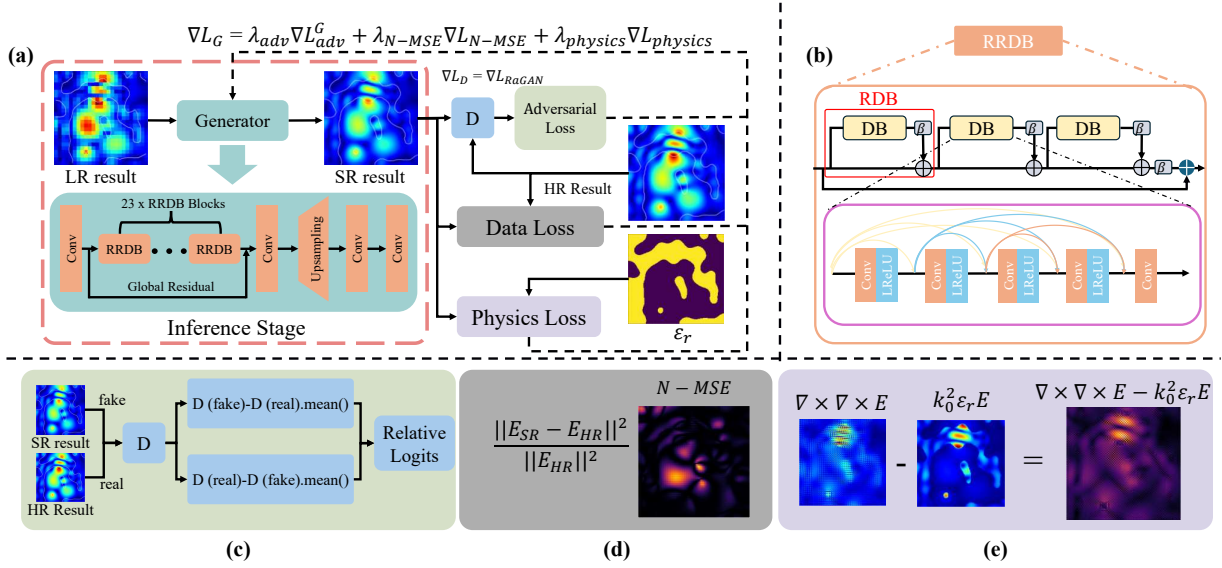


Fig. 2: (a) SuperPhys-Net model architecture for electromagnetic field super-resolution, demonstrating the complete training framework. (b) Detailed RRDB (Residual in Residual Dense Block) structure showing the hierarchical dense connections and residual learning mechanism. (c) Relativistic adversarial loss computation, where D denotes the discriminator network. (d) Data loss calculation. (e) Physics loss calculation.

Since coarse-grid and fine-grid simulations solve identical Maxwell’s equations using different spatial discretization schemes, we can establish a learning-based mapping \mathcal{F} that predicts fine-grid fields \mathbf{E}_f from coarse-grid data \mathbf{E}_c :

$$\mathbf{E}_f = \mathcal{F}(\mathbf{E}_c) \quad (4)$$

B. The Proposed SuperPhys-Net Framework

As shown in Fig. 1(c), our proposed framework offers an efficient pipeline for fine-grid EM simulations of nanophotonic devices with complex geometries. The simulation process utilizes a two-stage computational approach for effective EM field prediction. Initially, a standard FDFD solver conducts simulations on a coarse grid, yielding rapid initial field solutions. This coarse EM field data is then input into our SuperPhys-Net, a physics-informed SR network that accurately predicts and reconstructs fine-grid field distributions from the coarse-grid inputs, ensuring precise EM field predictions while adhering to fundamental physical principles. This two-stage approach significantly reduces the computational time compared to direct fine-grid FDFD simulations.

C. SuperPhys-Net Model Architecture

As shown in Fig. 2(a), our SuperPhys-Net adopts the ESRGAN framework, adapting its generator and discriminator architectures for EM field SR [29].

Generator Architecture: The generator follows the ESRGAN architecture adapted for complex EM field processing. It takes a 2-channel input representing real and imaginary components of coarse-grid EM fields and produces fine-grid outputs. This dual-channel design preserves both amplitude and phase information essential for accurate EM wave modeling.

The architecture comprises an initial convolution layer that maps the 2-channel input to 64 feature channels, followed by a feature extraction trunk containing 23 Residual-in-Residual Dense Blocks (RRDBs) with dense connectivity and growth parameter 32. The trunk is then processed through a convolution layer with global residual connections before bicubic upsampling with $2\times$ magnification and final reconstruction layers that output the complex EM field.

Each RRDB uses residual scaling (0.2) for stability, while dense connectivity (as illustrated in Fig. 2(b)) promotes gradient flow—crucial for EM applications where local field variations must satisfy global wave constraints. The deep 23-block architecture provides sufficient capacity to model complex relationships between EM field distributions across complex topological structures.

Discriminator Architecture: We implement a relativistic discriminator (RaGAN) that performs comparative evaluation rather than absolute classification for EM field SR. The base discriminator uses a deep convolutional architecture with progressive downsampling to extract multi-scale EM field features. The relativistic wrapper computes relative authenticity: $\text{real_logits} = D(\mathbf{E}_{\text{real}}) - \mathbb{E}[D(\mathbf{E}_{\text{fake}})]$ and $\text{fake_logits} = D(\mathbf{E}_{\text{fake}}) - \mathbb{E}[D(\mathbf{E}_{\text{real}})]$, where \mathbf{E}_{real} and \mathbf{E}_{fake} represent ground truth and generated EM fields respectively. This comparative approach provides more stable training dynamics and stronger gradient signals for EM field reconstruction, encouraging the generator to produce fields with more accurate physical details than standard adversarial training.

D. Loss Function

Our loss function integrates multiple components specifically designed for EM field SR, combining normalized pixel-

level accuracy with physics-informed constraints and adversarial learning objectives.

Relativistic Adversarial Loss: As illustrated in Fig. 2(c), we employ the relativistic average GAN (RaGAN) formulation following the ESRGAN framework for adversarial training. The generator adversarial loss is:

$$\mathcal{L}_{\text{adv}}^G = -\mathbb{E}[\log(\sigma(D_{\text{fake}} - \mathbb{E}[D_{\text{real}}]))] - \mathbb{E}[\log(1 - \sigma(D_{\text{real}} - \mathbb{E}[D_{\text{fake}}]))] \quad (5)$$

while the discriminator loss is:

$$\mathcal{L}_{\text{adv}}^D = -\mathbb{E}[\log(\sigma(D_{\text{real}} - \mathbb{E}[D_{\text{fake}}]))] - \mathbb{E}[\log(1 - \sigma(D_{\text{fake}} - \mathbb{E}[D_{\text{real}}]))] \quad (6)$$

where $D_{\text{real}} = D(\mathbf{E}_{\text{real}}) - \mathbb{E}[D(\mathbf{E}_{\text{fake}})]$ and $D_{\text{fake}} = D(\mathbf{E}_{\text{fake}}) - \mathbb{E}[D(\mathbf{E}_{\text{real}})]$, providing more stable training dynamics for complex EM field generation.

Normalized Complex Field Loss: As shown in Fig. 2(d), we use N-MSE as both the training objective and evaluation metric, which is proven to possess rotation invariance properties essential for accurate complex field distance measurement [12]. The normalization ensures scale-invariant optimization across EM field samples with varying magnitudes.

$$\mathcal{L}_{\text{N-MSE}}(\mathbf{E}_{\text{SR}}, \mathbf{E}_{\text{HR}}) = \frac{\|\mathbf{E}_{\text{SR}} - \mathbf{E}_{\text{HR}}\|_2^2}{\|\mathbf{E}_{\text{HR}}\|_2^2} \quad (7)$$

Physics-Informed Loss: Following Maxwell's equations in linear, isotropic, and non-magnetic media without free sources, the time-harmonic electric field $\mathbf{E}(\mathbf{r})$ satisfies the vector wave equation:

$$\nabla \times \nabla \times \mathbf{E}(\mathbf{r}) - k_0^2 \varepsilon_r(\mathbf{r}) \mathbf{E}(\mathbf{r}) = 0, \quad (8)$$

where $k_0 = 2\pi/\lambda$ is the free-space wavenumber at wavelength λ , and $\varepsilon_r(\mathbf{r}) = n^2(\mathbf{r})$ is the spatially varying relative permittivity related to the refractive index $n(\mathbf{r})$. Using the vector calculus identity

$$\nabla \times (\nabla \times \mathbf{E}) = \nabla(\nabla \cdot \mathbf{E}) - \nabla^2 \mathbf{E}, \quad (9)$$

Eq. (8) can be rewritten as

$$-\nabla^2 \mathbf{E} + \nabla(\nabla \cdot \mathbf{E}) - k_0^2 \varepsilon_r(\mathbf{r}) \mathbf{E} = 0. \quad (10)$$

For the 2D simulation case considered here, the structure is assumed invariant along the z -axis and composed of linear, isotropic, non-magnetic materials without free charges or currents. Under these assumptions, Maxwell's equations decouple into independent transverse electric (TE) and transverse magnetic (TM) polarizations. For TM polarization, the only nonzero electric-field component is $E_z(x, y)$, with $E_x = E_y = 0$. The governing equation reduces to the scalar Helmholtz equation:

$$\nabla^2 E_z + k_0^2 \varepsilon_r E_z = 0, \quad (11)$$

where $k_0 = 2\pi/\lambda$ is the free-space wavenumber, λ is the wavelength, and $\varepsilon_r(x, y)$ is the relative permittivity distribution. As shown in Fig. 2(e), our physics-informed loss is derived from this equation.

The physics loss is defined by the squared L_2 norm of the

residual of this equation applied to the SR field E_{SR} :

$$\mathcal{L}_{\text{physics}} = \|\nabla^2 E_{\text{SR}}(x, y) + k_0^2 \varepsilon_r(x, y) E_{\text{SR}}(x, y)\|_2^2. \quad (12)$$

In our experiment, the Laplacian $\nabla^2 E_{\text{SR}}$ is discretized using a high-order finite-difference stencil, while $\varepsilon_r(x, y)$ enters explicitly in the residual term to modulate the local wavenumber.

The total generator loss combines all components:

$$\mathcal{L}_G = \lambda_{\text{N-MSE}} \mathcal{L}_{\text{N-MSE}} + \lambda_{\text{adv}}^G \mathcal{L}_{\text{adv}}^G + \lambda_{\text{phys}} \mathcal{L}_{\text{physics}} \quad (13)$$

In our implementation, we set $\lambda_{\text{N-MSE}} = 1.0$ as the primary loss component for EM field reconstruction, $\lambda_{\text{adv}}^G = 5 \times 10^{-3}$ for adversarial training, and λ_{phys} as a tunable hyperparameter to balance the optimization contributions of different loss components. We deliberately exclude perceptual loss components designed for natural images, as VGG-based features are not suitable for complex EM field data.

IV. EXPERIMENTAL RESULTS

A. Experimental Setup

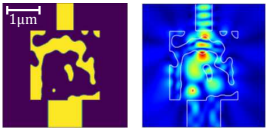
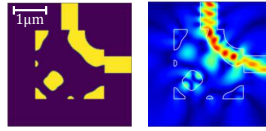
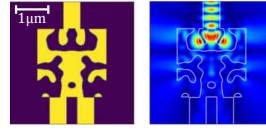
Simulation Configuration: We use MEEP [32], an open-source software package for EM simulation, to generate all training data. The computational domain spans $6.0 \times 6.0 \mu\text{m}^2$ with perfectly matched layers (PML) of thickness $1.0 \mu\text{m}$ implemented at all boundaries to suppress spurious reflections. All simulations are performed at the optical communication wavelength of $\lambda = 1.55 \mu\text{m}$. Wave excitation is achieved using an eigenmode source that launches the fundamental TM_{01} mode with a Gaussian temporal profile. All experiments were conducted on NVIDIA A800-SXM4 GPUs with 80GB memory.

Owing to the TM polarization of the source, the EM field exhibits specific properties: the electric field component \mathbf{E}_z is non-zero and constitutes the dominant longitudinal component, while the in-plane electric field components \mathbf{E}_x and \mathbf{E}_y are zero. Consequently, our analysis primarily focuses on the \mathbf{E}_z field distribution. Simulations are run until steady state is reached, defined as the point when the total field energy decays by 25 dB relative to its peak value, with a relative convergence threshold of 10^{-5} .

Device Benchmarks: To validate the performance and generalizability of our SuperPhys-Net framework, we employed three fundamental photonic components as benchmark devices with a minimum feature size and spacing of 110 nm. All benchmark devices incorporate identical $2.0 \mu\text{m} \times 2.0 \mu\text{m}$ design regions with distinct functionalities: **MC** performs TE_0 to TE_1 mode conversion, **WB** enables 90-degree waveguide bending, and **PS** achieves equal power splitting between dual outputs.

Dataset and Training Configuration: Our training dataset comprises 5,000 samples per device benchmark. Each sample consists of: (i) coarse-grid E_z fields (25 points/ μm) as input, (ii) fine-grid E_z fields (50 points/ μm) as ground truth, and (iii) fine-grid permittivity distribution ε_r for physics loss calculation. The 50 points/ μm resolution provides sufficient accuracy for capturing essential field features. SR reconstruction is performed exclusively on the pattern region, which represents

TABLE I: Comparison of validation error, test error and training time for various approaches.

Benchmarks	Model	Val error (10^{-2}) ↓	Test error (10^{-2}) ↓	Training Time (s) ↓
 Mode Converter	NeurOLight [11]	16.20	15.81	19292
	PACE [12]	12.25	12.73	30054
	Bicubic [30]	-	12.75	-
	SRCNN [31]	8.33	8.28	1036
	SRResNet [26]	5.59	5.60	2644
	SuperPhys-Net (This work)	3.25	3.25	14947
 Waveguide Bending	NeurOLight [11]	18.75	18.37	19121
	PACE [12]	14.62	14.43	30016
	Bicubic [30]	-	14.79	-
	SRCNN [31]	9.29	9.39	1040
	SRResNet [26]	6.54	6.57	2642
	SuperPhys-Net (This work)	4.06	4.03	14989
 Power Splitter	NeurOLight [11]	15.57	15.27	18957
	PACE [12]	11.57	11.22	31086
	Bicubic [30]	-	12.37	-
	SRCNN [31]	8.15	8.04	1047
	SRResNet [26]	5.59	5.59	2645
	SuperPhys-Net (This work)	3.25	3.22	14765

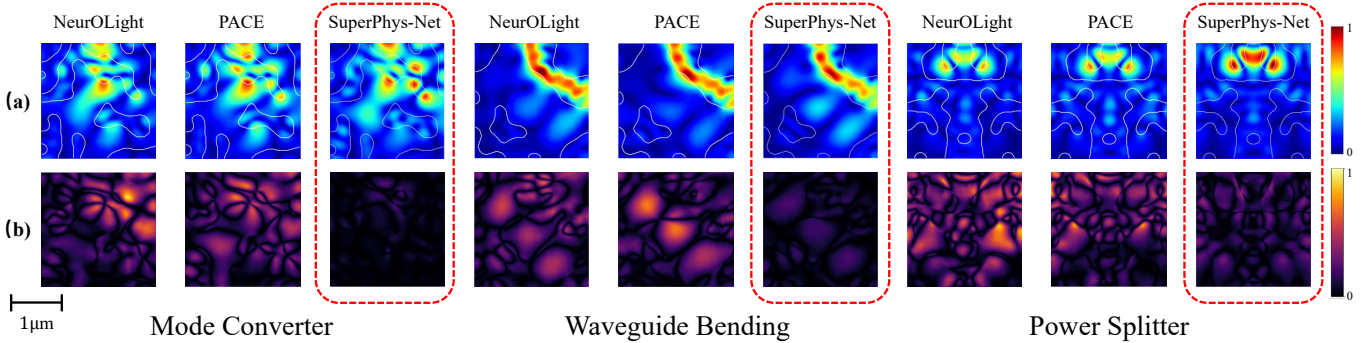


Fig. 3: Field prediction performance comparison. (a) Predicted electric field magnitude $|E_z|$ for NeurOLight, PACE, and SuperPhys-Net across three benchmarks. (b) Prediction error $|\Delta E_z|$ for the three methods.

the most computationally challenging area. For NeurOLight and PACE, we provide a Gaussian light source covering $0.4 \mu\text{m} \times 2 \mu\text{m}$ for mask field restoration. Each benchmark is trained independently using a 70%-15%-15% split for training, validation, and test sets, with batch size 12 for 150 epochs, and optimized using N-MSE as the learning objective.

Baseline Selection and Justification: Our comparative evaluation employs several baseline methods selected to represent different approaches relevant to EM field SR. NeurOLight [11] and PACE [12] represent pioneering neural operator-based approaches for accelerating FDFD simulation of photonic devices. PIC2O [13] is excluded from comparison as it specifically targets FDTD simulation rather than the FDFD approach employed in this work. Since our task is fundamentally an SR problem, we include additional baselines from the SR domain: bicubic interpolation [30] and classic CNN-based SR methods (SRCNN [31], SRResNet [26]). Diffusion models are excluded due to their substantial inference time requirements [33], which conflict with our computational efficiency objectives.

Performance Comparison: TABLE I shows that

TABLE II: Improvement in Performance with Physics Loss

Benchmark	Physics Loss	Val Err (10^{-2}) ↓	Test Err (10^{-2}) ↓
MC	×	3.84	3.84
	✓	3.25	3.25
WB	×	4.33	4.27
	✓	4.06	4.03
PS	×	3.52	3.52
	✓	3.25	3.22
Avg. Improvement		-9.76%	-9.84%

SuperPhys-Net achieves accuracy improvements ranging from 38.66% to 79.44% across all baseline methods, with 72.54% and 72.61% improvements on validation and test data, respectively, compared to the current state-of-the-art PACE model. Moreover, SuperPhys-Net requires approximately 50% less training time than PACE across all benchmarks. This combination of superior accuracy and computational efficiency makes it highly suitable for nanophotonic device simulations.

The unsatisfactory performance of baseline methods can be

TABLE III: Runtime Comparison

Benchmark	Runtime (s)		Runtime Reduction
	MEEP	SuperPhys-Net	
MC	5.34	1.34	74.91%
WB	5.46	1.27	76.74%
PS	5.56	1.30	76.62%
Average Runtime Reduction		76.09%	

attributed to several factors. NeurOLight and PACE, which are purely data-driven methods that depend entirely on neural networks, struggle to capture the complex relationships between device geometry and EM field distributions due to the intricate structures of nanophotonic devices. While bicubic interpolation effectively preserves low-frequency components, it fails to recover critical high-frequency details. Similarly, SRCNN and SRResNet generate overly smooth predictions that lack the fine-grid features essential for accurate field representation. Although CNN-based methods require less training time, their limited accuracy makes them insufficient for high-fidelity nanophotonic simulations. To illustrate the superior performance of our model, we visualize the EM field distributions predicted by various methods along with their errors relative to the ground truth in Fig. 3.

B. Improvement in Prediction Accuracy with Physics Loss

During training, the N-MSE loss serves as a strong constraint for model optimization by providing direct supervision on the desired EM field distributions. This data-driven component is essential, since pure PINNs relying solely on physics loss often struggle with convergence and may get trapped in poor local minima when solving Maxwell’s equations. The N-MSE loss acts as a crucial guidance mechanism, directing the optimization toward the correct solution space. To achieve optimal performance, we carefully tune the weight of the physics loss component. Through extensive experiments, we determined that a physics loss weight of 1×10^{-4} yields the best model performance, providing sufficient physical constraint without overwhelming the data-driven learning process.

The results in TABLE II demonstrate that physics-informed training reduces errors by 9.76% and 9.84% on validation and test sets, respectively. This consistent improvement across all three benchmarks validates our hybrid approach.

C. Computational Efficiency Evaluation

Given that SuperPhys-Net targets the acceleration of nanophotonic device simulations with complex topological structures, computational efficiency serves as a paramount evaluation criterion. We conducted runtime comparisons between our method and MEEP for generating fine-grid EM field distributions across three benchmark devices. To maintain experimental integrity, our reported runtime encompasses both the initial coarse-grid MEEP simulation and the subsequent SuperPhys-Net SR process. The results presented in Table III reveal significant computational savings, with an average runtime reduction of 76.09% across all benchmark devices.

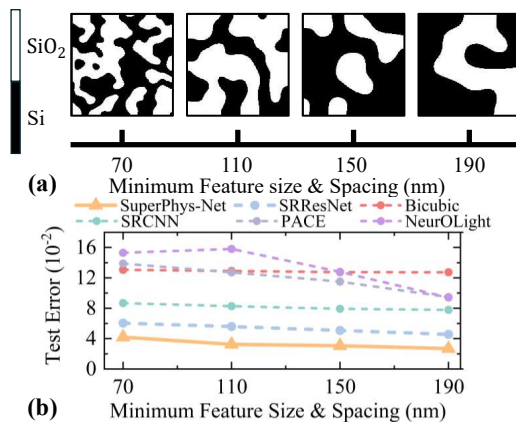


Fig. 4: (a) Representative nanophotonic device patterns generated with minimum feature sizes and spacing of 70nm, 110nm, 150nm, and 190nm. (b) Performance comparison of all baseline methods and SuperPhys-Net across different feature scales.

D. Generalization Performance across Feature Scales

To further investigate the generalization capability of our model, we conducted experiments with varying minimum feature sizes to evaluate the predictive performance of our approach against baseline models across different geometric scales. Using a specialized generation algorithm [34], we created device datasets with minimum feature sizes and spacing of 70nm, 110nm, 150nm, and 190nm, and performed EM simulations on each dataset. Examples of different feature sizes and spacing values are shown in Fig. 4(a).

The experimental results demonstrate that our model consistently maintains the lowest test error across all feature scales and significantly outperforms all baseline methods, as shown in Fig. 4(b). We observe that model performance degrades as the minimum feature size decreases, which can be attributed to the fact that smaller geometric features correspond to richer high-frequency components in the EM field distribution, thereby increasing the complexity of accurate field prediction.

V. CONCLUSION

In this work, we propose the SuperPhys-Net framework for EM simulations of nanophotonic devices with complex geometrical structures. Results show that our framework delivers substantial improvements, achieving 72.61% higher accuracy than the state-of-the-art method while reducing computational time by 76.09% compared to standard FDFD solvers. Our proposed method also demonstrates excellent generalizability, consistently outperforming baseline approaches across nanophotonic devices with varying dimensions.

VI. ACKNOWLEDGMENT

This work is supported by the Natural Science Foundation of Guangdong Province (No.2024A1515012438) and Nansha District Key Area S&T Scheme (No. 2024ZD007).

REFERENCES

- [1] S. Shekhar, W. Bogaerts, L. Chrostowski, J. E. Bowers, M. Hochberg, R. Soref, and B. J. Shastri, "Roadmapping the next generation of silicon photonics," *Nature Communications*, vol. 15, no. 1, p. 751, 2024.
- [2] Y. Shi, Y. Zhang, Y. Wan, Y. Yu, Y. Zhang, X. Hu, X. Xiao, H. Xu, L. Zhang, and B. Pan, "Silicon photonics for high-capacity data communications," *Photonics Research*, vol. 10, no. 9, pp. A106–A134, 2022.
- [3] F. Sunny, A. Mirza, M. Nikdast, and S. Pasricha, "Crosslight: A cross-layer optimized silicon photonic neural network accelerator," in *2021 58th ACM/IEEE design automation conference (DAC)*. IEEE, 2021, pp. 1069–1074.
- [4] Z. Liu, D. Zhu, L. Raju, and W. Cai, "Tackling photonic inverse design with machine learning," *Advanced Science*, vol. 8, no. 5, p. 2002923, 2021.
- [5] A. Y. Piggott, J. Petykiewicz, L. Su, and J. Vučković, "Fabrication-constrained nanophotonic inverse design," *Scientific reports*, vol. 7, no. 1, p. 1786, 2017.
- [6] C. Dory, D. Verduyck, K. Y. Yang, N. V. Sapro, A. E. Rugar, S. Sun, D. M. Lukin, A. Y. Piggott, J. L. Zhang, M. Radulaski *et al.*, "Inverse-designed diamond photonics," *Nature communications*, vol. 10, no. 1, p. 3309, 2019.
- [7] S. Molesky, Z. Lin, A. Y. Piggott, W. Jin, J. Vucković, and A. W. Rodriguez, "Inverse design in nanophotonics," *Nature Photonics*, vol. 12, no. 11, pp. 659–670, 2018.
- [8] A. Y. Piggott, J. Lu, K. G. Lagoudakis, J. Petykiewicz, T. M. Babinec, and J. Vučković, "Inverse design and demonstration of a compact and broadband on-chip wavelength demultiplexer," *Nature photonics*, vol. 9, no. 6, pp. 374–377, 2015.
- [9] H. Chen, Y. Ma, and Y. Tong, "Bi-level optimization accelerated drc-aware physical design automation for photonic devices," in *2025 Design, Automation & Test in Europe Conference (DATE)*. IEEE, 2025, pp. 1–7.
- [10] Y. Su, H. Chen, Y. Zang, Q. Hao, Y. Ma, and Y. Tong, "Machine learning-assisted design automation of integrated photonic devices," in *2025 International Symposium of Electronics Design Automation (ISED)*. IEEE, 2025, pp. 718–723.
- [11] J. Gu, Z. Gao, C. Feng, H. Zhu, R. Chen, D. Boning, and D. Pan, "NeuroLight: A physics-agnostic neural operator enabling parametric photonic device simulation," *Advances in Neural Information Processing Systems*, vol. 35, pp. 14 623–14 636, 2022.
- [12] H. Zhu, W. Cong, G. Chen, S. Ning, R. Chen, J. Gu, and D. Z. Pan, "Pace: Pacing operator learning to accurate optical field simulation for complicated photonic devices," *Advances in Neural Information Processing Systems*, vol. 37, pp. 67 535–67 555, 2024.
- [13] P. Ma, H. Yang, Z. Gao, D. S. Boning, and J. Gu, "Pic2o-sim: A physics-inspired causality-aware dynamic convolutional neural operator for ultra-fast photonic device time-domain simulation," *APL Photonics*, vol. 10, no. 3, 2025.
- [14] M. Raissi, P. Perdikaris, and G. E. Karniadakis, "Physics-informed neural networks: A deep learning framework for solving forward and inverse problems involving nonlinear partial differential equations," *Journal of Computational physics*, vol. 378, pp. 686–707, 2019.
- [15] J. Lim and D. Psaltis, "Maxwellnet: Physics-driven deep neural network training based on maxwell's equations," *Apl Photonics*, vol. 7, no. 1, 2022.
- [16] M. G. Mahmoud, A. S. Hares, M. F. O. Hameed, M. El-Azab, and S. S. Obayya, "Ai-driven photonics: Unleashing the power of ai to disrupt the future of photonics," *APL Photonics*, vol. 9, no. 8, 2024.
- [17] H. Feng, P. Hu, Y. Wang, D. Fan, T. Wu, and Y. Zhang, "Physics-informed super-resolution and forecasting method based on inaccurate partial differential equations and partial observation," *Physics of Fluids*, vol. 37, no. 6, 2025.
- [18] K. Fukami, K. Fukagata, and K. Taira, "Super-resolution analysis via machine learning: a survey for fluid flows," *arXiv preprint arXiv:2301.10937*, 2023.
- [19] F. Li, X. Jia, D. Fraser, and A. Lambert, "Super resolution for remote sensing images based on a universal hidden markov tree model," *IEEE Transactions on Geoscience and Remote Sensing*, vol. 48, no. 3, pp. 1270–1278, 2009.
- [20] S. Lei, Z. Shi, and Z. Zou, "Super-resolution for remote sensing images via local-global combined network," *IEEE Geoscience and Remote Sensing Letters*, vol. 14, no. 8, pp. 1243–1247, 2017.
- [21] P. Shu, R. W. Aslam, I. Naz, B. Ghaffar, D. E. Kucher, A. Qudsoos, D. Raza, M. Abdullah-Al-Wadud, and R. M. Zulqarnain, "Deep learning-based super-resolution of remote sensing images for enhanced ground-water quality assessment and environmental monitoring in urban areas," *IEEE Journal of Selected Topics in Applied Earth Observations and Remote Sensing*, 2025.
- [22] S. K. Jha, V. Gupta, P. J. Sharma, A. Mishra, and S. Joshi, "Deep learning super-resolution for temperature data downscaling: a comprehensive study using residual networks," *Frontiers in Climate*, vol. 7, p. 1572428, 2025.
- [23] C.-H. Chiang, Z.-H. Huang, L. Liu, H.-C. Liang, Y.-C. Wang, W.-L. Tseng, C. Wang, C.-T. Chen, and K.-C. Wang, "Climate downscaling: a deep-learning based super-resolution model of precipitation data with attention block and skip connections," *arXiv preprint arXiv:2403.17847*, 2024.
- [24] B. B. Moser, F. Raue, S. Frolov, S. Palacio, J. Hees, and A. Dengel, "Hitchhiker's guide to super-resolution: Introduction and recent advances," *IEEE Transactions on Pattern Analysis and Machine Intelligence*, vol. 45, no. 8, pp. 9862–9882, 2023.
- [25] D. C. Lepcha, B. Goyal, A. Dogra, and V. Goyal, "Image super-resolution: A comprehensive review, recent trends, challenges and applications," *Information Fusion*, vol. 91, pp. 230–260, 2023.
- [26] C. Ledig, L. Theis, F. Huszár, J. Caballero, A. Cunningham, A. Acosta, A. Aitken, A. Tejani, J. Totz, Z. Wang *et al.*, "Photo-realistic single image super-resolution using a generative adversarial network," in *Proceedings of the IEEE conference on computer vision and pattern recognition*, 2017, pp. 4681–4690.
- [27] H. Li, S. Liu, and E. L. Tan, "Super resolution deep learning network for finite-difference time-domain simulations," *IEEE Antennas and Wireless Propagation Letters*, 2024.
- [28] J. Seo, I. Kim, and J. Seok, "Grid-wise simulation acceleration of the electromagnetic fields of 2d optical devices using super-resolution," *Scientific reports*, vol. 13, no. 1, p. 435, 2023.
- [29] X. Wang, K. Yu, S. Wu, J. Gu, Y. Liu, C. Dong, Y. Qiao, and C. Change Loy, "Esrgan: Enhanced super-resolution generative adversarial networks," in *Proceedings of the European conference on computer vision (ECCV) workshops*, 2018, pp. 0–0.
- [30] R. Keys, "Cubic convolution interpolation for digital image processing," *IEEE transactions on acoustics, speech, and signal processing*, vol. 29, no. 6, pp. 1153–1160, 2003.
- [31] C. Dong, C. C. Loy, K. He, and X. Tang, "Image super-resolution using deep convolutional networks," *IEEE transactions on pattern analysis and machine intelligence*, vol. 38, no. 2, pp. 295–307, 2015.
- [32] A. F. Oskooi, D. Roundy, M. Ibanescu, P. Bermel, J. D. Joannopoulos, and S. G. Johnson, "Meep: A flexible free-software package for electromagnetic simulations by the fdtd method," *Computer Physics Communications*, vol. 181, no. 3, pp. 687–702, 2010.
- [33] B. B. Moser, A. S. Shanbhag, F. Raue, S. Frolov, S. Palacio, and A. Dengel, "Diffusion models, image super-resolution, and everything: A survey," *IEEE Transactions on Neural Networks and Learning Systems*, 2024.
- [34] H. Chen, M. Zhang, and Y. Tong, "Always-feasible photonic inverse design with a differentiable conditional design generator," *ACS Photonics*, vol. 11, no. 10, pp. 4461–4471, 2024.